

Long-range chaotic Brillouin optical correlation domain analysis with more than one million resolving points

Yahui Wang^{a,b,†}, Xinxin Hu,^{a,†} Lintao Niu,^a Hui Liu,^a Jianzhong Zhang,^a and Mingjiang Zhang^{a,b,c,*}

^aTaiyuan University of Technology, Ministry of Education, Key Laboratory of Advanced Transducers and Intelligent Control System, Taiyuan, China

^bTaiyuan University of Technology, College of Physics, Taiyuan, China

^cShanxi-Zheda Institute of Advanced Materials and Chemical Engineering, Taiyuan, China

Abstract. We propose and experimentally demonstrate a long-range chaotic Brillouin optical correlation domain analysis by employing an optimized time-gated scheme and differential denoising configuration, where the number of effective resolving points largely increases to more than one million. The deterioration of the chaotic Brillouin gain spectrum (BGS) and limitation of sensing range owing to the intrinsic noise structure, resulting from the time delay signature (TDS) and nonzero background of chaotic laser, is theoretically analyzed. The optimized time-gated scheme with a higher extinction ratio is used to eliminate the TDS-induced impact. The signal-to-background ratio of the measured BGS is enhanced by the differential denoising scheme to furthest remove the accumulated nonzero noise floor along the fiber, and the pure chaotic BGS is ulteriorly obtained by the Lorentz fit. Ultimately, distributed strain sensing along a 27.54-km fiber with a 2.69-cm spatial resolution is experimentally demonstrated, and the number of effective resolving points is more than 1,020,000.

Keywords: chaos; distributed fiber sensing; stimulated Brillouin scattering; long-range sensing.

Received Jan. 16, 2023; revised manuscript received Mar. 31, 2023; accepted for publication Apr. 27, 2023; published online May 18, 2023.

© The Authors. Published by SPIE and CLP under a Creative Commons Attribution 4.0 International License. Distribution or reproduction of this work in whole or in part requires full attribution of the original publication, including its DOI.

[DOI: [10.1117/1.APN.2.3.036011](https://doi.org/10.1117/1.APN.2.3.036011)]

1 Introduction

Distributed optical fiber sensors (DOFSs) have a promising future due to their applications in the field of structure monitoring, disaster warning, intelligent Internet of Things, and so on.^{1–3} The DOFS based on Brillouin scattering has widely been used because of the linear relationship between the Brillouin frequency shift (BFS) with temperature and strain.⁴ So far, the distributed Brillouin sensors can be classified into frequency,^{5,6} time,^{7,8} and correlation domains^{9,10} according to different operating principles. The measurement range (MR) of Brillouin optical time domain analysis (BOTDA) has been promoted beyond 100 km with a spatial resolution (SR) of several meters.^{11,12} However, the sensing distance of SR-enhanced sensors, such as the differential pulse–width pair,¹³ transient pump pulse,¹⁴ and monopulse

self-difference,¹⁵ is limited to thousands of meters resulting from the poor signal-to-noise ratio (SNR) and nonlocal system response. Compared to BOTDA sensors, the Brillouin optical correlation domain analysis (BOCDA) could circumvent the limitation of the phonon lifetime on pulse width to enable random accessibility of the sensing positions with an SR at the centimeter or even millimeter level.¹⁶ Therefore, the BOCDA has great potential to achieve precise positioning and high accuracy in long-range measurement.¹⁷

Several methods have been inspired to enlarge the MR of BOCDA sensors. The number of effective resolving points (N_{eff}) is defined as the ratio of the MR to SR, which has been adopted as a merit parameter to evaluate the DOFS performance.¹⁸ In sinusoidal-wave frequency-modulation (sine-FM) schemes, differential measurement,¹⁹ double modulation,²⁰ and time-domain data processing²¹ were proposed to prevent the gain interference from adjacent periodic correlation peaks (CPs), where the maximum N_{eff} has been expanded to one million over an MR

*Address all correspondence to Mingjiang Zhang, zhangmingjiang@tyut.edu.cn

[†]These authors contributed equally to this work.

of 10.5 km.²⁰ Moreover, the MR of phase-coded BOCDA was extended by combining phase coding and pump pulse modulation,^{22–24} where the multiple CPs were concurrently interrogated and the N_{eff} was improved to beyond two million along a 17.5-km fiber.²⁴ To compensate for the loss of pump pulse due to the intrinsic fiber loss and stimulated Brillouin scattering (SBS) interaction, the distributed Raman amplification²⁵ or wideband Brillouin amplification²⁶ was introduced to achieve a 52.1-km sensing distance with about 744,000 resolving points, which is the largest-MR BOCDA at present.²⁵ However, in the sine-FM and phase-coded systems, the scanning of periodic CPs is achieved by adjusting the frequency of sinusoidal signal or the rate of phase sequence. The CP width is slightly changed during the localization process, leading to the worsening in SR.^{21,24} Consequently, the SR would gradually deteriorate by increasing the MR, which limits the further expansion of resolving points.¹⁷ In addition, the modulation devices with higher bandwidth and several extrinsic generators are required, with the cost and complexity increasing inevitably.

Recently, a chaotic laser, as a new partially coherent source,²⁷ has been successfully introduced into the BOCDA.^{28–32} The noise-like property of chaotic laser ensures that there is a sole CP along the fiber, so the MR can be extended due to the gain anti-interference in principle. The broadband characteristic makes it easy to achieve a millimeter-level SR, which is only dependent on the chaos bandwidth and will not change with the sensing distance. Consequently, the chaotic BOCDA has performed forceful competitiveness in coupling the large MR and high SR. For example, a time-gated chaotic BOCDA scheme has been proposed to suppress the noise background, induced by time delay signature (TDS) of chaos, and promote the sensing distance to 10.2 km with resolving points of more than 110,000.²⁹ Then the bandwidth-enhanced chaotic laser, which can be generated easily via the simplest single-feedback loop structure without extra complex modulation, has been applied to achieve an SR of 3.5 mm and resolving points of more than 47,000.³⁰ However, similar to the sine-FM or phase-coded protocols, the feeble gain and accumulated residual noise also make it difficult to enable a massive number of resolution points based on a longer sensing range.¹⁷

In this work, aiming at the distinctive operating principle and noise mechanism, where the incompletely suppressed noise structure is cumulated due to the leakage of the pulsative pump and the secondary SBS interaction is still stimulated as a result of the weakly correlated transmission of the continuous probe, the chaotic BOCDA with an optimized time-gated scheme and differential denoising configuration is first proposed to effectively extend the MR and promote the resolving points. The deterioration of chaotic Brillouin gain spectrum (BGS) due to the intrinsic TDS of the chaotic laser and the nonzero noise floor is analyzed theoretically. Then the elimination of the TDS-induced noise structure is verified in simulation by the optimized time-gated scheme with higher extinction ratio (ER). The differential denoising configuration is further introduced to improve the signal-to-background ratio (SBR) of the chaotic BGS by reducing the ghost noise and off-peak background along the fiber under test (FUT). Moreover, the standard deviation of BFS at the end of the FUT decreases to 2.27 MHz by processing with a Lorentz fit. In experiments, the distributed strain sensing along a 27.54-km sensing fiber with a 2.69-cm SR is demonstrated, where the number of effective resolving points exceeds 1,020,000.

2 Principle

2.1 Construction of Chaotic BGS

In conventional chaotic BOCDA, the schematic illustration of the BGS generation is shown in Fig. 1(a). It is only within the CP that a stable SBS acoustic field can be excited to stimulate a sharp intrinsic BGS (red line in the FUT) along the whole FUT. The sidelobe peaks at TDS positions are similar to the central CP and the secondary sharp BGSs (blue line in the FUT) could be generated, which provide dominant components in the noise structure. Moreover, the off-peak noise (black line in the FUT) introduced by the nonzero background at the positions away from the peaks is gradually broadened and accumulated, which is weaker and negligible for short-range sensing. Therefore, the measured BGS, interrogated from the power variation of probe, is constructed with the gain from the CP and noise structure from all the off-CP sections of the FUT. Consequently, the difference in BFS at CP and off-CP sections will result in a bimodal BGS, which are referred to as the main peak and subpeak. In previous works, the main-subpeak ratio (MSPR) is induced to determine the quality of chaotic BGS, in which the negatively correlated relationship between the MSPR and TDS magnitude has been experimentally verified.³¹ Although the impact of TDS on BGS contour could be eliminated by increasing the delay time τ_d , the long-feedback-cavity chaos, whose length is less than that of FUT, is more effective for short-range sensing.³²

Further, a time-gated scheme has been proposed to optimize the chaotic BGS for a long-range sensing system.²⁹ The chaos probe wave remains continuous while the pump wave is modulated into pulse with a duration τ_p , which is smaller than τ_d and larger than the phonon lifetime τ , so that the probe wave only interacts with the pump pulse during τ_p . As shown in Fig. 1(b), the pulse ER is defined as the ratio of the peak power to base power of pulsative chaos, $ER = 20 \cdot \log(V_{\text{peak}}/V_{\text{base}})$. Due to the shortened interaction time, the SBS interaction is mainly stimulated within the CP and the noise gain along the FUT could be largely inhibited. Theoretically, as the principal illustration in Fig. 1(c), the measured gain consists of the local BGS within the CP (red line in the FUT) and the off-peak background outside the CP within the pulse width (black line in the FUT). When the pulsative chaos passes through the off-CP positions, the probe wave is secondarily amplified due to weak correlation characteristics.

There are two aspects that should be considered for the noise mechanism. On the one hand, the residual interactions between the probe wave and the leakage wave of pulse pump are introduced at the off-peak positions and gradually accumulated along the FUT, which is closely related to the pulse ER. In long-range sensing, when the pulse ER is inferior, the extra-SBS interactions between the pulse base and continuous probe wave will dominate and an incomplete suppression of noise SBS acoustic field, generated by the TDS peaks, will also result. On the other hand, the ghost interactions between the high-level section of the pulse pump and the off-CP section of the probe wave could be stimulated by the trend of continuous attenuation. As the blue dotted lines depict in Fig. 1(c), due to the weakly correlated characteristic in the transmission process, the noise gains at ghost peak positions (TDS-dependent) and off-peak background are inevitably excited and accumulated. With respect to these two mechanisms, the measured BGS consists of the main gain

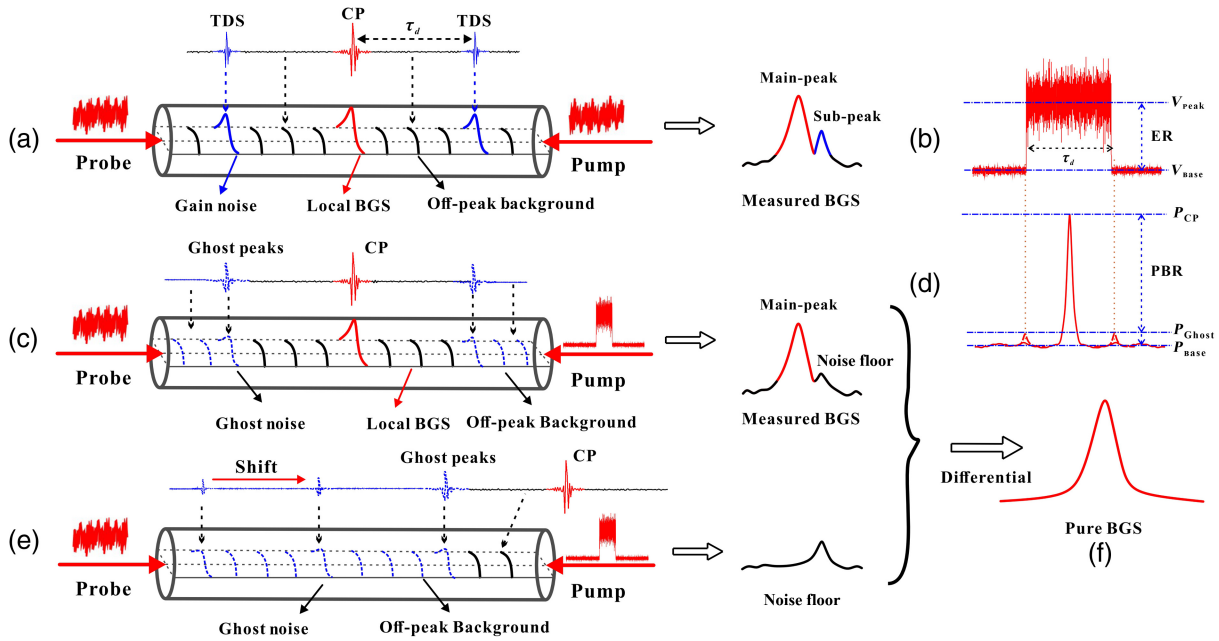


Fig. 1 Schematic illustration of the chaotic BGS construction. (a) Conventional chaotic BOFDA; (b) definition of pulse ER in chaos-based scheme; (c) time-gated chaotic BOFDA system; (d) definition of the chaos PBR; (e) measurement of the noise floor along the FUT; (f) pure chaotic BGS after differential denoising.

within CP and the noise floor due to the ghost peaks and off-peak amplifications.

To estimate the intensity of Brillouin gain within CP, the peak-to-base ratio (PBR) is defined as the logarithmic ratio of the central CP to the mean value of the nonzero base on the autocorrelation curve, $PBR = 10 \cdot \log(P_{CP}/P_{base})$. Remarkably, the P_{base} should be replaced by the P_{ghost} when the intensity of ghost peak cannot be ignored. Therefore, a TDS-suppression chaotic laser is initially employed to achieve a higher PBR; meanwhile, a higher ER of pump pulse is essential to weaken the impact of the ghost peak. Although the PBR and ER are synergistically optimized to attenuate the ghost noise and off-peak background, the noise floor of chaotic BGS is almost impossible to eliminate completely, which will turn into another pivotal noise source in long-range sensing.

Further, a differential denoising scheme is proposed; the principle is shown in Fig. 1(e). By increasing the delay time of the probe wave, the central CP can be addressed at arbitrary positions along the FUT. When the delay length is twice as long as the FUT, the CP is removed from the FUT; meanwhile, the cumulative noise floor of the entire fiber could be reserved and measured. Therefore, by analyzing the difference between the measured BGS and the noise floor, a pure BGS, consisting of only a sharp gain signal, could be obtained theoretically, as shown in Fig. 1(f). The differential denoising method is principally different from the differential measurement,^{19,20} in which the pure gain signal is obtained by changing the correlation characteristic and taking the difference between the phase modulation on and off.

2.2 Theoretical Analysis of Gain Measurement

In a long-range pulse-based sensing system with an SR of <2 m, it can be assumed that the gain or loss experienced

by the probe wave in a brief local interaction is small ($<5\%$), and the protocol operates in a small gain condition.³³ For a fixed frequency difference, the local Brillouin gain of the probe wave at an arbitrary position along the FUT can be expressed as

$$G(z) = \frac{g_B(z)}{A_{eff}} \cdot P_p(z) \cdot \Delta z, \quad (1)$$

where $g_B(z)$ is the local Brillouin gain coefficient, A_{eff} is the effective mode area, $P_p(z)$ is the peak power of pump pulse, and Δz is the SR. The gain coefficient $g_B(z)$ is considered to be constant over the interaction length Δz and be positive in the Brillouin gain configuration.

Assuming that the interaction has a negligible effect on the power of pump and probe waves in small-gain condition, the pump pulse launched at the near end ($z = 0$) simply experiences an exponential decay during the propagation and can be expressed as $P_p(z) = P_{pi} \exp(-\alpha z)$, where α is the linear attenuation coefficient and $P_{pi} = P_p(0)$ is the input peak power of the pump pulse at $z = 0$. Therefore, $G(z)$ can be further expressed as

$$G(z) = \frac{g_B}{A_{eff}} \cdot P_{pi} \exp(-\alpha z) \cdot \Delta z. \quad (2)$$

The local sensor response, which is the amount of power transferred from the pump pulse to the probe wave, is $\Delta P_s(z) = P_s(z)G(z)$.³⁴ Similarly, the small gain approximation makes the probe wave launched at the far end ($z = L$) negligibly affected by the interaction and can be expressed as $P_s(z) = P_{si} \exp[-\alpha(L - z)]$, where $P_{si} = P_s(L)$ is the input power of the probe wave. Because the amplified power of probe wave at position z is measured at $z = 0$, another exponential

decay process is experienced and the sensor response measured at $z = 0$ is given by

$$\begin{aligned}\Delta P_s^0(z) &= P_{si} \exp[-\alpha(L - z)] \exp(-\alpha z) \times G(z) \\ &= \frac{g_B}{A_{\text{eff}}} P_{pi} P_{si} \exp[-\alpha(L + z)] \Delta z.\end{aligned}\quad (3)$$

In the time-gated chaotic BOCDA, the gain process of the probe wave is confined to the pulse duration. Therefore, it is reasonable to assume that this protocol operates in a small-gain condition. In addition, the intensity of the acoustic field is proportional to the autocorrelation coefficient, so the intensity of off-peak positions is much weaker than that of the central CP. Taking into consideration the PBR of chaos and the pulse ER, the sensor responses at the near end can be given by

$$\begin{aligned}\Delta P_{s1}^0(z) &= \frac{g_B}{A_{\text{eff}}} P_{pi} P_{si} \exp[-\alpha(L + z)] \cdot \left[\xi \frac{\tau_p}{T} + \frac{1}{\xi} \left(1 - \frac{\tau_p}{T} \right) \right] \\ &\quad \cdot \eta \frac{\tau_c}{\tau_p} \cdot L_c,\end{aligned}\quad (4)$$

$$\begin{aligned}\Delta P_{s2}^0(z) &= \frac{g_B}{A_{\text{eff}}} P_{pi} P_{si} \exp[-\alpha(L + z)] \cdot \xi \frac{\tau_p}{T} \cdot \frac{1}{\eta} \left(1 - \frac{\tau_c}{\tau_p} \right) \\ &\quad \cdot (L_{\text{eff}} - L_p),\end{aligned}\quad (5)$$

$$\begin{aligned}\Delta P_{s3}^0(z) &= \frac{g_B}{A_{\text{eff}}} P_{pi} P_{si} \exp[-\alpha(L + z)] \cdot \frac{1}{\xi} \left(1 - \frac{\tau_p}{T} \right) \\ &\quad \cdot \left[\eta \frac{\tau_c}{\tau_p} (L_p - L_c) + \frac{1}{\eta} \left(1 - \frac{\tau_c}{\tau_p} \right) L_{\text{eff}} \right],\end{aligned}\quad (6)$$

where $\Delta P_{s1}^0(z)$, $\Delta P_{s2}^0(z)$, and $\Delta P_{s3}^0(z)$ are the pure Brillouin gain, the ghost noise, and the off-peak background, respectively. ξ and η represent the values of ER and PBR. $L_p = V_g \tau_p / 2$ is the spatial length of the pulse width. $L_c = V_g \tau_c / 2$ is the spatial width of the central CP, where τ_c is the coherence time of the chaotic laser. $L_{\text{eff}} = [1 - \exp(-\alpha L)] / \alpha$ is the effective length of the FUT.

For a certain PBR and L_p , the main Brillouin gain is generated from the SBS interaction within L_c , between the high-level pump wave and the highly correlated section of the probe wave $G_m \propto \xi(\tau_p/T) \cdot \eta(\tau_c/\tau_p) \cdot L_c$, although the measured one at $z = 0$ gradually decreases as the sensing distance increases. And the side interactions $G_s \propto (1/\xi)(1 - \tau_p/T) \cdot \eta(\tau_c/\tau_p) \cdot L_c$, due to the leakage wave of pulse pump, also contribute to the gain process, whose intensity is highly dependent on the ER. In addition, outside the L_p , a series of ghost peaks are stimulated by the secondary correlation and the resulting ghost noise, $G_g \propto \xi(\tau_p/T) \cdot (1/\eta)(1 - \tau_c/\tau_p) \cdot (L_{\text{eff}} - L_p)$, could be sufficiently limited by using a high-PBR chaotic laser. For the off-peak noise, the residual background within the L_p , $G_r \propto (1/\xi)(1 - \tau_p/T) \cdot \eta(\tau_c/\tau_p) \cdot (L_p - L_c)$, and the randomly fluctuating background due to the pump base, $G_f \propto (1/\xi)(1 - \tau_p/T) \cdot (1/\eta)(1 - \tau_c/\tau_p) \cdot L_{\text{eff}}$, are continuously accumulated over the whole FUT, which are even greater

than the pure gain in the long-range system. Obviously, the higher ER and PBR are synchronously essential to obtain a superior gain signal, although the noise floor cannot be eliminated completely. By moving the L_c out of the FUT properly, the ghost noise and the accumulated off-peak background could be measured to the greatest extent and then the optimized chaotic BGS could be obtained in the differential denoising scheme. Moreover, the pump pulse depletion and the nonlocal effect would also lead to a distortion in BGS measurement and an error increase in BFS.³⁵

2.3 Optimization of Chaotic BGS

To optimize the chaotic BGS, the effect of the pulse ER is first analyzed. As shown in Fig. 2(a), the continuous chaotic laser is experimentally modulated into pulse waves with different ERs by an electro-optic modulator (EOM) or a semiconductor optical amplifier (SOA). The ER of the SOA-based scheme is 52.40 dB, which is about 17.53 dB higher than that of the EOM-based scheme. Further, the chaotic BGSs with or without temporal gating are simulated in a short-range sensing system, as illustrated in Fig. 2(b). Notably, the linewidth of BGS is slightly broadened due to the effect of intensity modulation on the beat spectrum in the time-gated configurations. In the simulation, the main BFS of the FUT is 10.73 GHz, and a 10 cm-long event section with a BFS of 10.64 GHz is placed at the end. When the central CP is located at the event section, the simulated BGS in the continuous chaos-based system performs bimodal, whose BFSs of the main peak and subpeak are 10.64 and 10.73 GHz, respectively. The subpeak of the BGS is mainly caused by the TDS, and the SBR is merely 4.01 dB. In the EOM-based scheme, the subpeak is largely suppressed, with an increased SBR of 8.42 dB. In the SOA-based scheme, the subpeak is almost completely inhibited, and the SBR is improved to 11.02 dB, which is 7.01 and 2.60 dB higher than that of the continuous chaos-based and EOM-based schemes, respectively. The impact of chaos TDS on BGS measurement has theoretically been chiefly weakened by the high-ER time-gated scheme.

However, the optimized BGS remains a feeble subpeak and a palpably trapezoidal noise structure because of the ghost noise and off-peak background, which will progressively intensify and be the main noise mechanism in the long-range sensing system. As depicted in Fig. 2(c), in a system, the chaotic BGSs at different positions of 100-km FUT are simulated and the SBRs are further analyzed. Compared to the position of $z = 0$, the noise background is gradually accumulated again with the increase of sensing range, and the SBR decreases to 3.10 dB at the position of $z = L/2$. Finally, at the bottom of the FUT, the SBR is severely worsened to -2.16 dB, implying that the feeble gain signal would nearly submerge into the noise floor induced by the accumulative off-CP amplifications. The differential denoising method is tentatively proposed to reduce the deterioration of the off-CP background. The simulation results of the differential denoising scheme are depicted in Fig. 2(d). According to Eqs. (4)–(6), the measured noise floor (black curve) almost coincides with the base structure of the BGS (red curve), and the denoised BGS presents a practically perfect Lorenz shape. Therefore, the optimization of the chaotic BGS could be implemented using an SOA-based time-gated scheme and a differential denoising configuration synchronously, and then the sensing distance would be effectively extended.

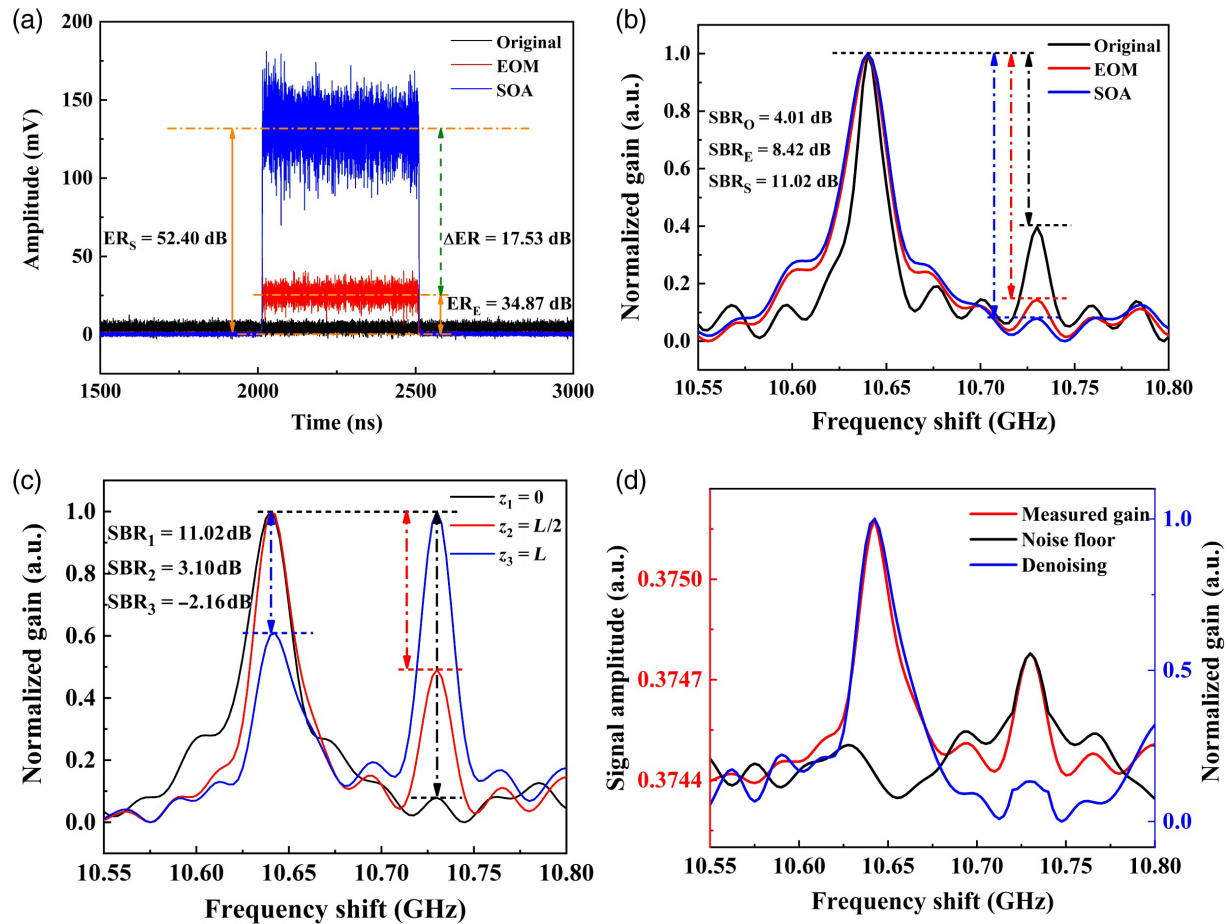


Fig. 2 Optimization of the chaotic BGS in simulation. (a) Time series under different pulse modulation methods; (b) measured BGSs with or without time gating; (c) BGSs at different positions in long-range system; (d) schematic of differential denoising method.

3 Experiments

3.1 Measurement of Chaotic BGS

The experimental setup of the proposed long-range chaotic BOCDA is shown in Fig. 3. A chaotic laser with the linewidth Δf of 0.032 nm is employed as the light source and the theoretical SR of this protocol is ~ 2.5 cm. Remarkably, the PBR is 9.84 dB with a suppressed ghost peak at 544.9 ns. The output chaos is divided into two branches by a 90/10 optical coupler. The upper branch (90%), as the probe wave, is modulated in the suppress-carrier, double-sideband format by an EOM, driven by a microwave generator (MWG) to match the BFS of the fiber. The double-sideband modulation could provide a higher gain intensity and a weakened nonlocal effect in long-range sensing system.²⁸ Then the probe wave passes through a programmable optical delay generator (PODG), which is used to localize the CP in the FUT. After being amplified by a continuous erbium-doped fiber amplifier (EDFA), the probe wave is injected into the FUT through an optical isolator, where the power is about 7.5 dBm. A polarization scrambler is used to prevent polarization-dependent fading of the SBS interaction.

The lower branch (10%) is used as pump wave, which is modulated into pulse wave by an SOA. According to the τ_d of 544.9 ns, the τ_p of 500 ns is selected to inhibit the

TDS-dependent noise floor and optimize the gain intensity. The repetition rate is ~ 3.6 kHz, depending on the round-trip time in the FUT. The pump wave is then amplified to 25.6 dBm (peak power) by a pulse EDFA and counterpropagated to the FUT through an optical circulator. Finally, the amplified Stokes wave, filtered by the optical bandpass filter, is detected by a photodetector and sampled by a lock-in amplifier in real time. As the bottom view shows, the FUT is composed of two single-mode-fiber (SMF) sections, whose length of the first section (SMF1) is about 27.53 km; the second one (SMF2) is 8.0 m.

The chaotic BGSs with different modulation methods in this proposed system are measured and compared. Figures 4(a) and 4(b) show the BGSs at two positions of 13.80 and 27.53 km along the FUT, which are located at different fiber sections. The black and red curves represent the BGSs measured in the EOM and SOA modulated system, respectively. It can be seen that the center BFSs of BGSs are 10.73 and 10.64 GHz, and the noise structure of BGS in the SOA-based scheme is significantly lower. Concretely, in the middle section of the FUT, the SBR of SOA-based scheme is 2.39 dB, which is 1.80 dB larger than that of the EOM-based scheme. However, as shown in Fig. 4(b), the SBR of EOM-based scheme is merely -1.07 dB, indicating that the intensity of the noise structure even exceeds the SBS gain, and thus the event section cannot

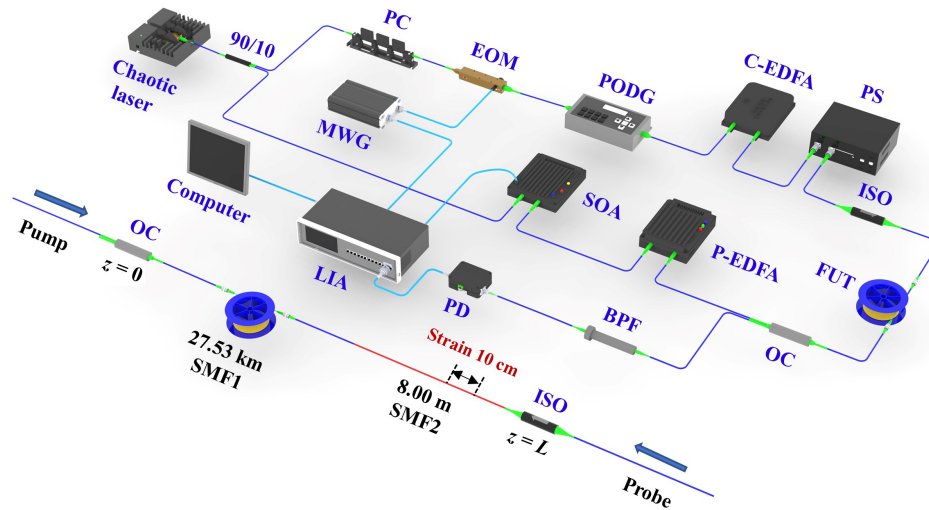


Fig. 3 Experimental setup of the proposed long-range chaotic BOCDA.

be distinguished at the far end of the FUT. In contrast, the SBR of the SOA-based scheme is 0.36 dB, and the gain signal is still greater than the noise floor. The differential denoising is further applied to reduce the accumulated noise background, and the SBRs of BGSs are improved from 2.39 to 4.98 dB (blue curves) or from 0.36 to 1.86 dB.

Figure 4(c) shows the SBR as a function of the fiber position. The SBR of the EOM-based scheme starts to be <0 dB when the MR is longer than 18.80 km, meaning that the SBS gain is submerged in the noise floor. Compared to the traditional time-gated scheme, the obvious increments of SBR, 4.39 dB at the middle and 2.93 dB at the end of the FUT, could be obtained in this proposed protocol, and the effective MR could be longer than 27.53 km. Notably, as the noise background depicted in Fig. 2(b), several additional noise mechanisms, such as incompletely suppressed off-CP background, inherent fluctuations of chaos power, and systematic noise during photoelectric or phase-amplitude conversion, would be further removed to improve the SBR and enhance the MR expectantly.

3.2 Measurement of BFS Distribution

Figures 5(a) and 5(b) show the BGS map along the FUT in this long-range chaotic BOCDA. After the differential denoising, the SMF1 at the front of the FUT and the SMF2 at the position of

later than 27.53 km, can be properly identified with the ordinary BFS of around 10.73 and 10.64 GHz, respectively. As illustrated in Fig. 2, a 10 cm-long strain section is located at the end of the FUT, which is stretched with about $1000 \mu\epsilon$, and that section can be recognized with the BFS of ~ 10.69 GHz.

However, the identification of BFS is seriously disturbed by the incompletely suppressed noise floor, especially at the SMF2 section. As the purple curves depict in Figs. 4(a) and 4(b), the Lorentz fit is introduced to further optimize the chaotic BGSs to reduce the randomly fluctuating floor. Ulteriorly, the BGSs along the FUT are improved and the superior BFS distributions are obtained. As illustrated in Figs. 5(c) and 5(d), the SMF2 and the strain section, even the connection between the SMF1 and the SMF2, are clearer to distinguish, where the noise floor could be assumed to be completely eliminated.

To ascertain the effect of the Lorentz fit on BFS accuracy, the BFS distributions at the end of the SMF2 before and after the Lorentz fit are measured, respectively. Figure 6(a1) shows the reconstructed BFSs after differential denoising, where the red solid line performs the mean value of 10.639 GHz and the red dashed line performs the standard deviation of 2.98 MHz. In order to evaluate the BFS more accurately, the BFS fluctuation at this section is measured by 30 Bernoulli experiments; the corresponding result is shown in Fig. 6(a2). The mean value is 10.639 GHz with a standard deviation of 2.94 MHz, which

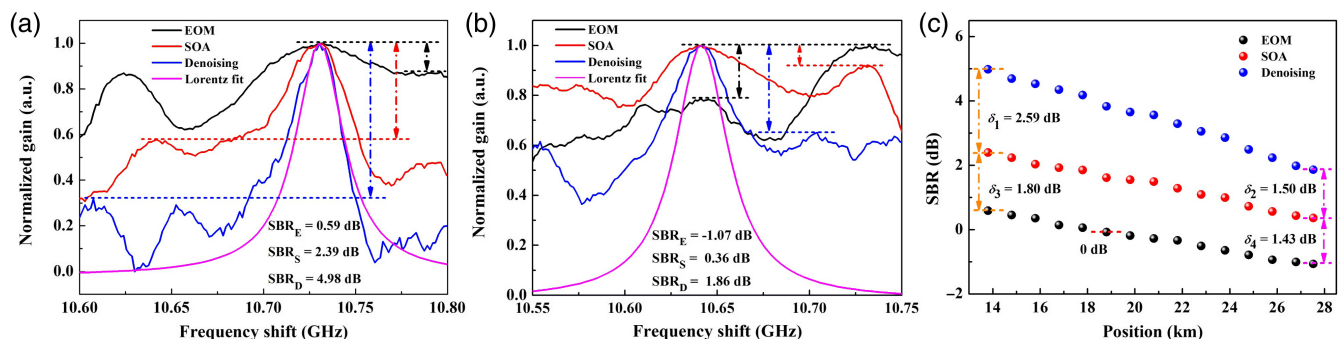


Fig. 4 The BGSs under different schemes at two positions along the FUT. (a) 13.80 km and (b) 27.53 km. (c) The SBR as a function of the fiber position.

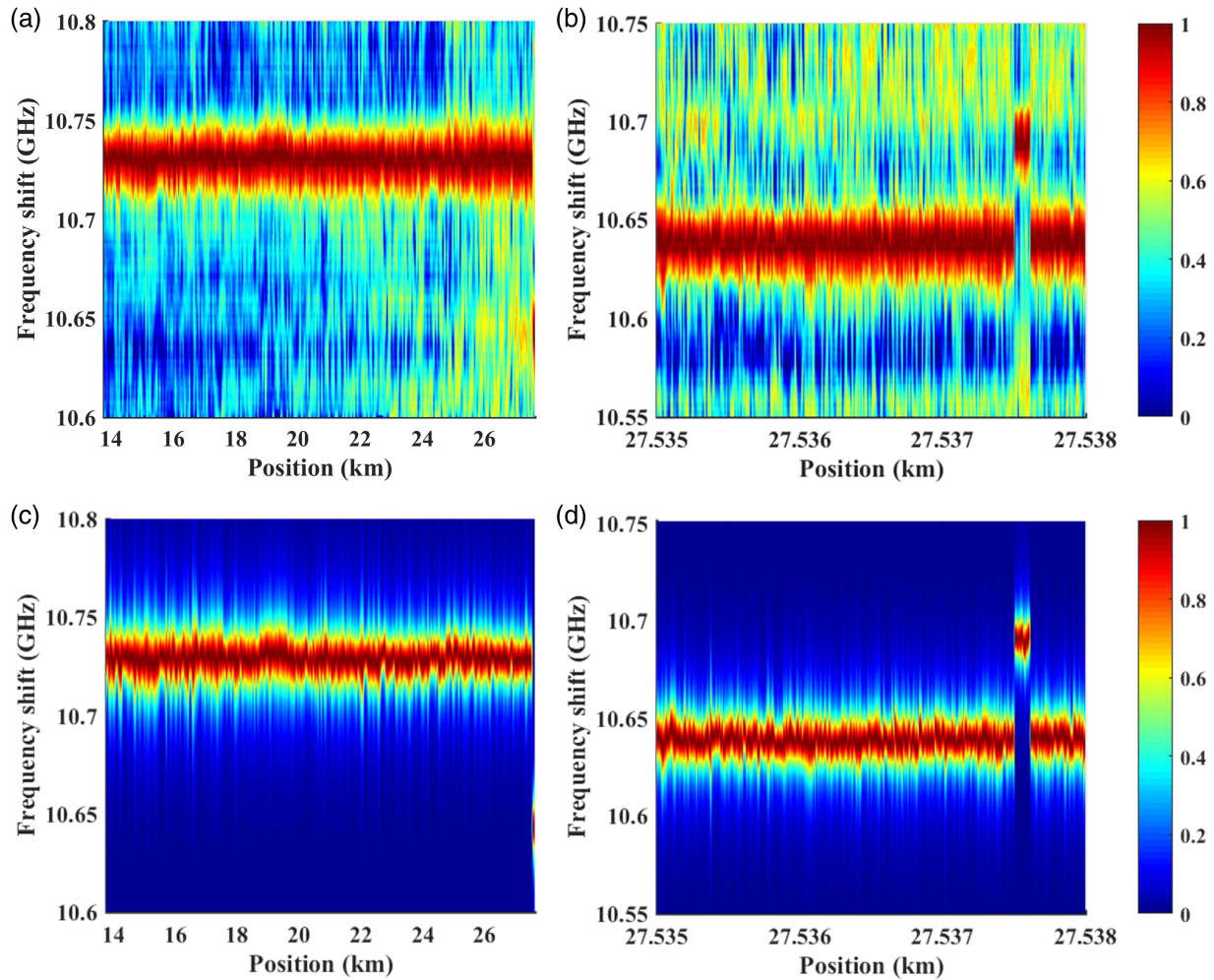


Fig. 5 The BGS map along (a) the second half of the FUT or (b) the SMF2 without Lorentz fit. The BGS map along (c) the second half of the FUT or (d) the SMF2 with Lorentz fit.

almost coincides with that of the single measurement. After the Lorentz fit, the mean value and standard deviation are further obtained and plotted in Figs. 6(b1) and 6(b2). The central BFSs remain at 10.639 GHz, while the standard deviation decreases from 2.98 to 2.33 MHz in the single measurement and from 2.94 to 2.27 MHz in the independent repeated measurement. Therefore, the Lorentz fit can slightly reduce the standard deviation of the reconstructed BFSs and suppress the impact of noise floor on the BFS accuracy. Due to the inherent broadband BGS and the incompletely suppressed noise floor, the measurement accuracy of BFS is slightly lower, which could be further promoted using a phase-chaos laser, aperiodic code, and distributed amplification.

3.3 Determination of Resolving Points

To demonstrate the strain dependence of BFS in the proposed configuration, the strain section is stretched from 0 to 3000 $\mu\epsilon$ with an interval of 500 $\mu\epsilon$. The single CP is shifted with a 3 cm step near the strain section by adjusting the PODG. The distribution of BFSs is shown in Fig. 7(a), where the event section could be clearly identified by the BFS variation of three specific positions. As the linearly fitting curves depicted in Fig. 7(b), the BFS-strain coefficients of the three positions are 0.0502, 0.0528,

and 0.0512 MHz/ $\mu\epsilon$, respectively, and the mean value is around 0.0514 MHz/ $\mu\epsilon$, which is adopted as the reference value.

The SR of the chaotic BOCDA can be obtained by the value of 10% to 90% of the rise- and fall-time equivalent length for the event segment.²⁸ Figure 8 shows the BFS distribution at the end of SMF2, measured with a 1 cm step, where the stretching strain is set to 1000 $\mu\epsilon$. Remarkably, the BFS distribution of the strain section is densely measured by moving the CP with a 0.25 cm step. It is clearly seen from the zoomed view that the BFSs at the strain part are completely separate from the original segment. The rise- and fall-time equivalent lengths are 2.73 and 2.65 cm, respectively; therefore, the SR of this scheme can approximately approach 2.69 cm along the 27.54-km FUT, indicating that the resolving points are going beyond 1,020,000.

4 Discussion

The main advantage of the chaotic BOCDA is that a millimeter-level SR, independent of the large MR, could be obtained without requiring higher-bandwidth modulators.^{28–32} This scheme enables point-by-point distributed positioning by utilizing the PODG, resulting in a time-consuming measurement process. Although the total time for a BGS measurement is only 3.0 s, it takes a long time to measure all the resolving points

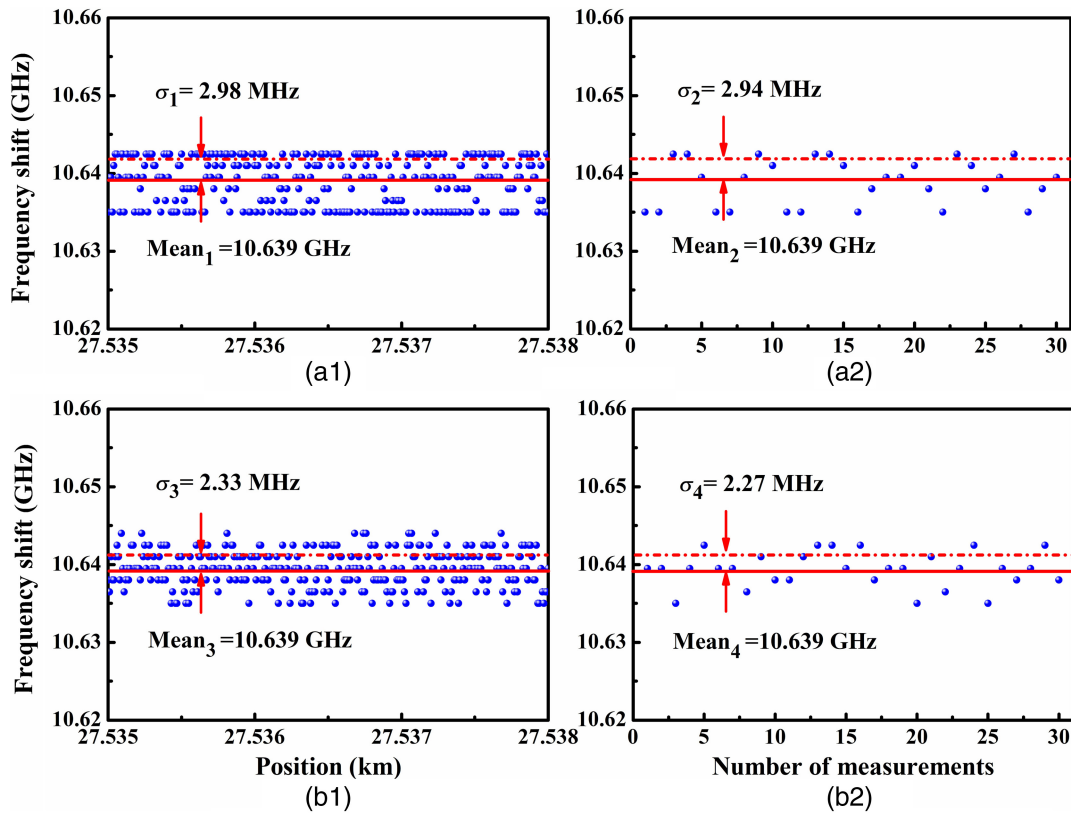


Fig. 6 The BFS accuracy at the SMF2 with different data processing methods. Standard deviation (a1) of single measurement or (a2) of the 30 independent repeated measurements before Lorentz fit; standard deviation (b1) of single measurement or (b2) of the 30 independent repeated measurements after Lorentz fit.

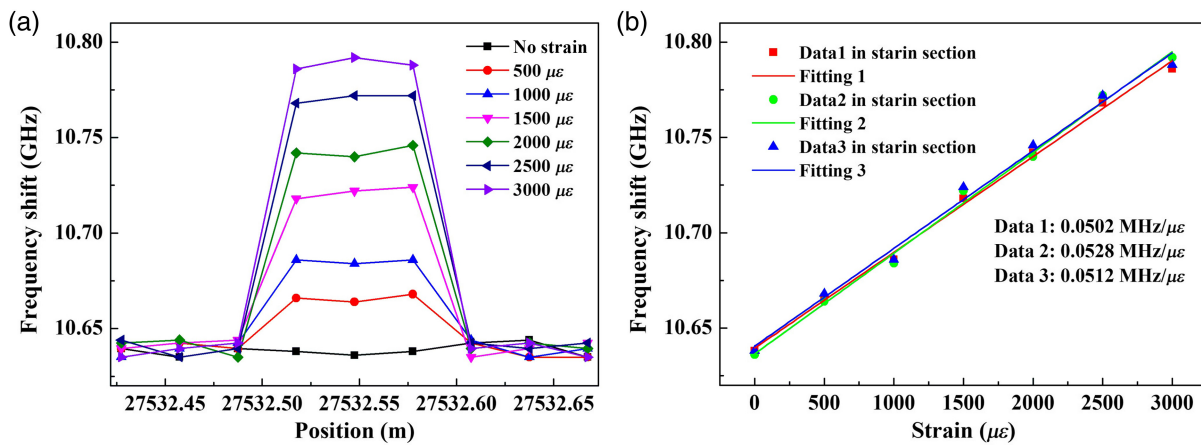


Fig. 7 (a) The BFS distribution near 10 cm strain section under different strains applied; (b) the BFS as a function of the applied strain.

on the FUT, which is unacceptable in practical applications. Using the higher-speed MWG and oscilloscope for frequency sweeping and data sampling, the measurement time could be marginally improved. Furthermore, the time-domain data processing method, recently proposed in the sine-FM and phase-coded systems,^{21–24} would be applied to the chaotic BOCDA for simultaneously interrogating multiple positions.

Additionally, several ameliorations would be further conducted to upgrade the performance of chaotic BOCDA. In the time-gated scheme, the MR is also limited by the depletion of pump pulse due to intrinsic fiber loss (0.2 dB/km in SMF at 1550 nm) and the SBS interaction, whereas the initial power is restricted by the modulation instability and nonlocal effects.^{33–35} The distributed Raman amplification could be introduced to

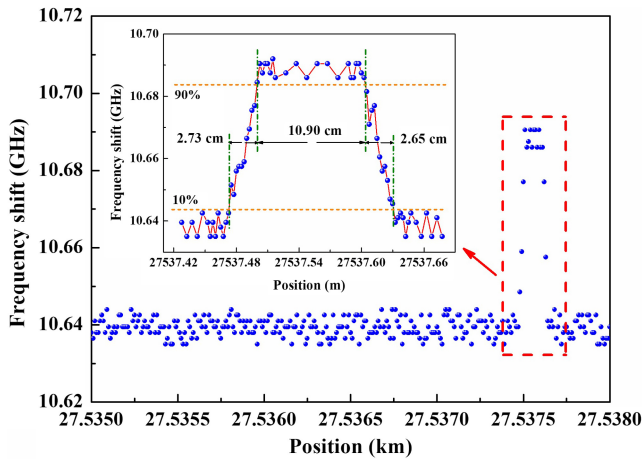


Fig. 8 The BFS distribution at the SMF2 and the zoomed view near the strain section.

provide a progressive spatial gain along the FUT. In addition, the SNR of the chaotic BOCDA is severely deteriorated due to the inherent fluctuation of the chaos power in the process not only of the gain generating but also of the power sampling. The phase-chaos laser, featuring a Gaussian-shaped broadband in the optical spectrum (i.e., randomness in phase), and standard fluctuation in power sequence, could be employed as the laser source to improve the measurement SNR ulteriorly.

5 Conclusion

We have demonstrated a long-range chaotic BOCDA enhanced using the optimized time-gated scheme and differential denoising configuration, where the effective resolving points are greatly enhanced to more than one million. The elimination of TDS is verified by the high-ER time-gated scheme both in simulation and experiment. The introduction of the differential denoising scheme effectively improves the SBR of chaotic BGS by suppressing the noise floor along the fiber. Additionally, the standard deviation of BFS at the end of the FUT is further reduced to ± 2.27 MHz by the Lorentz fit. Finally, the distributed strain sensing with an SR of 2.69 cm along the 27.54-km MR is experimentally achieved, and the number of resolving points is more than 1,020,000. This protocol has obtained prior merit in coupling the resolving points and sensing distance and provided a method for high-performance DOFS in health monitoring of the large-scale structure.

Acknowledgments

This work was supported by the National Natural Science Foundation of China (Grant Nos. 62205233, 62075151, and 62105234), the Fundamental Research Program of Shanxi Province (Grant No. 202103021223041), and Shanxi-Zheda Institute of Advanced Materials and Chemical Engineering. The authors declare no conflicts of interest.

References

1. P. Jousset et al., "Fibre optic distributed acoustic sensing of volcanic events," *Nat. Commun.* **13**, 1753 (2022).
2. J. Li and M. J. Zhang, "Physics and applications of Raman distributed optical fiber sensing," *Light Sci. Appl.* **11**, 128 (2022).

3. J. B. Murray, A. Cerjan, and B. Redding, "Distributed Brillouin fiber laser sensor," *Optica* **9**(1), 80–87 (2022).
4. P. Lu et al., "Distributed optical fiber sensing: review and perspective," *Appl. Phys. Rev.* **6**(4), 041302 (2019).
5. C. Karapanagiotis et al., "Distributed humidity fiber-optic sensor based on BOFDA using a simple machine learning approach," *Opt. Express* **30**(8) 12484–12494 (2022).
6. A. Minardo et al., "Proposal of Brillouin optical frequency-domain reflectometry (BOFDR)," *Opt. Express*, **24**(26), 29994–30001 (2016).
7. X. Y. Bao, Z. C. Zhou, and Y. Wang, "Review: distributed time-domain sensors based on Brillouin scattering and FWM enhanced SBS for temperature, strain and acoustic wave detection," *Photonix* **2**(1), 14 (2021).
8. X. Z. Sun et al., "Genetic-optimised aperiodic code for distributed optical fibre sensors," *Nat. Commun.* **11**, 5774 (2020).
9. J. H. Youn and K. Y. Song, "Brillouin optical correlation domain analysis using orthogonally polarized probe sidebands," *J. Lightwave Technol.* **40**(3), 894–899 (2022).
10. A. Zadok et al., "Random-access distributed fiber sensing," *Laser Photonics Rev.* **6**(5), L1–L5 (2012).
11. Y. K. Dong et al., "150 km fast BOTDA based on the optical chirp chain probe wave and Brillouin loss scheme," *Opt. Lett.* **43**(19) 4679–4682 (2018).
12. M. A. Soto, J. A. Ramirez, and L. Thevenaz, "Intensifying the response of distributed optical fibre sensors using 2D and 3D image restoration," *Nat. Commun.* **7**, 10870 (2016).
13. B. Z. Wang et al., "High-performance optical chirp chain BOTDA by using a pattern recognition algorithm and the differential pulse-width pair technique," *Photonics Res.* **7**(6), 652–658 (2019).
14. D. W. Zhou et al., "Millimeter-level recognition capability of BOTDA based on a transient pump pulse and algorithm enhancement," *Opt. Lett.* **46**(14), 3440–3443 (2021).
15. Q. Zhang et al., "Centimeter-level spatial resolution Brillouin optical time domain analyzer using mono-pulse self-difference," *Opt. Lett.* **47**(19), 5008–5011 (2021).
16. M. Matsumoto and S. Akai, "High-spatial-resolution Brillouin optical correlation domain analysis using short-pulse optical sources," *J. Lightwave Technol.* **37**(24), 6007–6014 (2019).
17. Y. H. Wang and M. J. Zhang, "Recent progress in long-range Brillouin optical correlation domain analysis," *Sensors* **22**(16), 6062 (2022).
18. J. H. Jeong et al., "Bidirectional measurement for Brillouin optical correlation domain analysis," *Opt. Express* **20**(10), 11091–11096 (2012).
19. J. H. Jeong et al., "Differential measurement scheme for Brillouin optical correlation domain analysis," *Opt. Express* **20**(24), 27094–27101 (2012).
20. Y. H. Kim, K. Lee, and K. Y. Song, "Brillouin optical correlation domain analysis with more than 1 million effective sensing points based on differential measurement," *Opt. Express* **23**(26), 33241–33248 (2015).
21. G. Ryu et al., "Brillouin optical correlation domain analysis enhanced by time-domain data processing for concurrent interrogation of multiple sensing points," *J. Lightwave Technol.* **35**(24), 5311–5316 (2017).
22. D. Elooz et al., "High-resolution long-reach distributed Brillouin sensing based on combined time-domain and correlation-domain analysis," *Opt. Express* **22**(6), 6453–6463 (2014).
23. Y. London et al., "Brillouin optical correlation domain analysis addressing 440 000 resolution points," *J. Lightwave Technol.* **34**(19), 4421–4429 (2016).
24. A. Denisov, M. A. Soto, and L. Thevenaz, "Going beyond 1000000 resolved points in a Brillouin distributed fiber sensor: theoretical analysis and experimental demonstration," *Light Sci. Appl.* **5**, e16074 (2016).
25. G. Ryu et al., "50 km-range Brillouin optical correlation domain analysis with first-order backward distributed Raman

- amplification,” *J. Lightwave Technol.* **38**(18), 5199–5204 (2020).
26. Y. Zhou et al., “Long-range high-spatial-resolution distributed measurement by a wideband Brillouin amplification-boosted BOCDA,” *J. Lightwave Technol.* **40**(16), 5743–5751 (2022).
 27. Y. Guo et al., “Ultrafast and real-time physical random bit extraction with all-optical quantization,” *Adv. Photonics* **4**(3), 035001 (2022).
 28. J. Z. Zhang et al., “Chaotic Brillouin optical correlation domain analysis,” *Opt. Lett.* **43**(8), 1722–1725 (2018).
 29. J. Z. Zhang et al., “Time-gated chaotic Brillouin optical correlation domain analysis,” *Opt. Express* **26**(13), 17597–17607 (2018).
 30. Y. H. Wang et al., “Millimeter-level-spatial-resolution Brillouin optical correlation-domain analysis based on broadband chaotic laser,” *J. Lightwave Technol.* **37**(15), 3706–3712 (2019).
 31. L. Zhao et al., “Effect of chaotic time delay signature on Brillouin gain spectrum in the slope-assisted chaotic BOCDA,” *Opt. Express* **28**(12), 18189–18201 (2020).
 32. L. Zhao et al., “Improvement of strain measurement accuracy and resolution by dual-slope-assisted chaotic Brillouin optical correlation domain analysis,” *J. Lightwave Technol.* **39**(10), 3312–3318 (2021).
 33. L. Thévenaz, S. F. Mafang, and J. Lin, “Effect of pulse depletion in a Brillouin optical time-domain analysis system,” *Opt. Express* **21**(12), 14017–14035 (2013).
 34. M. A. Soto and L. Thévenaz, “Modeling and evaluating the performance of Brillouin distributed optical fiber sensors,” *Opt. Express* **21**(25), 31347–31366 (2013).
 35. H. Iribas et al., “Effects of pump pulse extinction ratio in Brillouin optical time-domain analysis sensors,” *Opt. Express* **25**(22), 27896–27912 (2017).

Yahui Wang received his PhD in optics engineering from Taiyuan University of Technology (TYUT) in 2021. He is an assistant research fellow at TYUT. His research interests include chaotic laser and its Brillouin distributed fiber sensing.

Xinxin Hu received her BS and MS degrees in optical engineering from the TYUT in 2019 and 2022, respectively. She is currently working toward her PhD. Her research interests mainly focus on distributed Brillouin optical fiber sensing.

Lintao Niu received her BS degree in optoelectronic information science and engineering from Taiyuan University of Technology (TYUT) in 2021. She is pursuing her PhD at TYUT. Her current research interests include Brillouin distributed fiber sensing.

Hui Liu received her MS degree in optics engineering from TYUT in 2016. She is pursuing her PhD at TYUT. Her current research interests include Brillouin distributed fiber sensing.

Jianzhong Zhang received his PhD from TYUT in 2012. He is a professor at the Key Laboratory of Advanced Transducers and Intelligent Control System of TYUT. His research interests are in the areas of sensors, optical fiber sensing, and engineering application.

Mingjiang Zhang received his PhD in optics engineering from Tianjin University in 2011. He was a visiting scholar at the University of Ottawa, Canada in 2016. He is a professor and PhD supervisor at TYUT. His current research interests include photonic integrated chaotic laser and distributed optical fiber sensing. He also serves as a reviewer for journals of the IEEE, OSA, and Elsevier organizations.